GEOPHYSICS, VOL. 87, NO. 4 (JULY-AUGUST 2022); P. WB69–WB79, 10 FIGS.
10.1190/GEO2021-0602.1

DOI:10.1190/geo2021-0602.1

Drone-mounted ground-penetrating radar surveying: Flight-height considerations for diffraction-based velocity analysis

Adam D. Booth[1] and Tiffany M. Koylass[1]

ABSTRACT

Recent studies highlight the potential of the drone platform for ground-penetrating radar (GPR) surveying. Most guidance for optimizing drone flight heights is based on maximizing the image quality of target responses, but no study yet considers the impact on diffraction traveltimes. Strong GPR velocity contrasts across the air-ground interface introduce significant refraction effects that distort diffraction hyperbolas and introduce errors into diffraction-based velocity analysis. The severity of these errors is explored with synthetic GPR responses, using ray- and finite-difference approaches, and a field GPR data set acquired over a sequence of diffracting features buried up to 1 m depth. Throughout, GPR antennas with 1000 MHz center frequency are raised from the ground to heights <0.9 m (i.e., 0–3 times the wavelength in air). Velocity estimates are within +10% of modeled values (spanning from 0.07 to 0.13 m/ns) if the antenna height is within 1/2 wavelength in air above the ground surface. Greater heights reduce diffraction curvature, damaging velocity precision, and masking diffractions against a background of subhorizontal reflectivity. Field data highlight further problems of the drone-based platform, with data dominated by reverberations in the air gap and reduced spatial resolution of wavelets at target depth. We suggest that a drone-based platform is unsuitable for diffraction-based velocity analysis, and any future drone surveys are benchmarked against ground-coupled data sets.

INTRODUCTION

Ground-penetrating radar (GPR) is one of several geophysical systems to be considered for deployment on a drone-based platform. GPR is an established near-surface survey technique, using radio-wave energy to image a variety of geologic, hydrologic, and anthropogenic targets in the upper few meters of the subsurface (Annan, 2005). Most often, the antennas of a GPR system remain closely coupled with the ground surface but the growing availability and affordability of drone technology have prompted experimentation with drone-based GPR deployments.

Drones offer logistical advantages for rugged, dangerous, and/or inaccessible terrains, e.g., over water courses (Lane, 2019; Edemsky et al., 2021), at sites contaminated with unexploded ordnance (Cerquera et al, 2017; García-Fernández et al., 2020; Šipoš and Gleich, 2020), or over crevassed glacier fields (Mankoff et al., 2020). Even for practical terrains, an autonomous drone following a preprogrammed flight path (Hammack et al., 2020) improves efficiency by allowing surveyors to deploy other equipment simultaneously (e.g., systems requiring manual installation, such as seismic and/or resistivity methods). Although drone-based GPR surveys are subject to at least two sets of legislation that regulate drone operations (e.g., Valentine, 2019) and GPR emissions (e.g., Ofcom, 2019), several recent studies have demonstrated the advantages of the acquisition platform (Cerquera et al., 2017; Chandra and Tanzi, 2018; García-Fernández et al., 2020; Edemsky et al., 2021).

When benchmarking against conventional ground-coupled deployments, assessments of drone-based GPR data typically consider the impact on recorded wavelet amplitudes. For air-launched systems, the GPR energy entering the subsurface is diminished by reflectivity losses at the air-ground interface (García-Fernández et al., 2020) but other factors vary as a function of the drone flight height, and these include

1) increased geometric spreading, with antennas positioned further from the target (García-Fernández et al., 2020);

Manuscript received by the Editor 16 September 2021; revised manuscript received 13 February 2022; published ahead of production 4 May 2022; published online 27 June 2022.
[1]University of Leeds, Institute of Applied Geoscience, School of Earth and Environment, Leeds, UK. E-mail: a.d.booth@leeds.ac.uk (corresponding author); tiffany_mariah@hotmail.com.

DOI:10.1190/geo2021-0602.1

2) interference between reflections from the air-ground interface, and those from within the subsurface (Diamanti and Annan, 2017; Edemsky et al., 2021); and
3) poorer spatial resolution given the more rapid defocussing of the GPR beam as it travels through air (Diamanti and Annan, 2013, 2017), and the vulnerability to artifacts from above-surface scatterers.

The experience of vehicle-mounted GPR surveys (e.g., Saarenketo and Scullion, 2000; Eriksen et al., 2004; Zan et al., 2016) can provide a foundation for height considerations, but these often use horn antennas to maximize radiation in the target direction (usually downward). For any given center frequency, horn antennas tend to be bulkier than bow-tie systems (Pieraccini et al., 2017) hence, with accompanying batteries and control units, may exceed the payload of the drone. Furthermore, most experiments with drone-based GPR aim to mount an existing commercial system on the drone and most of these have a bow-tie or dipole design. The issues listed previously may therefore represent widespread design considerations but recommendations for flight height remain disparate, variously suggesting any height between 0.5 and 1.5 times the dominant wavelength of the radar wavelet in air (e.g., Diamanti and Annan, 2017; García-Fernández et al., 2018, 2020; Šipoš and Gleich, 2020). However, Smith (1984) suggests that the antenna coupling is poor when antennas are elevated by more than 0.1 times the wavelength in air, indicating that these larger conventions could be problematic.

Having noted these amplitude effects and the research effort to understand them, this paper investigates the impact of flight height on traveltime relationships expressed in recorded data and how they impact diffraction-based velocity analysis. A starting assumption, when comparing with ground-based data, may be that the reflections in drone-based data are shifted late according to the additional traveltime through the air gap. This may be reasonable for specular reflectivity, but refraction effects at the air-ground interface can cause distortions to the appearance of diffraction hyperbolas (Causse, 2004). This is especially problematic for engineering and archaeological applications where, for example, targets are often detected using diffraction responses and, furthermore, their curvature is used to determine subsurface velocities (e.g., for migration and time-to-depth conversion). Velocities also may be converted to dielectric permittivity, to inform hydrologic and engineering quantities such as water content and pavement density (Bradford et al., 2009; Diamanti et al, 2017; St. Clair and Holbrook, 2017). The limitations of hyperbolic velocity analysis, and the equivalent issues in seismic reflection processing (e.g., Alkhalifah, 1997), will be familiar to many in the community but, to date, there has been no study to explore the magnitude of velocity errors for a drone-based GPR system. It is therefore worth exploring the feasibility of diffraction-based velocity analysis for this novel survey platform.

Using ray-based and finite-difference synthetic analyses, we show the severity of these distortions as the height of drone-mounted antennas is changed and demonstrate the impact on diffraction-based velocity analysis. Our synthetics are complemented with field data, representing drone acquisition using antennas mounted on a height-adjustable frame. These data suggest that there would be significant difficulty in even recognizing diffraction hyperbolas in a drone-based data set, potentially precluding efforts to improve velocity characterization. Finally, we advise on the situations in which "fly low" or "fly high" scenarios may be preferable.

DIFFRACTION TRAVELTIMES AND VELOCITY RELATIONSHIPS

The traveltime $t(x - x_0)$ of a diffraction hyperbola from a point-source target is

$$t(x - x_0) = \sqrt{t_0^2 + \frac{4(x - x_0)^2}{v_{\text{rms}}^2}}, \quad (1)$$

where x is the midpoint position between common-offset GPR antennas, x_0 is the surface position vertically above the diffractor, t_0 is the two-way traveltime of diffracted arrivals at x_0, and v_{rms} is the root-mean-square velocity. These terms, and the hyperbolic $t(x - x_0)$ relationship they describe, are shown schematically for the ground-based raypath model in Figure 1. Assuming that the drone-mounted antennas are flown at height h above a subsurface with constant velocity v_{sub}, v_{rms} is the traveltime weighted average between v_{sub} and the velocity of the GPR wavelet through air ($v_{\text{air}} = 0.3$ m/ns):

$$v_{\text{rms}} = \sqrt{\frac{v_{\text{sub}}^2(t_0 - t_{\text{air}}) + v_{\text{air}}^2 t_{\text{air}}}{t_0}}, \quad (2)$$

where t_{air} is the two-way traveltime ($= 2h/v_{\text{air}}$) through the air gap at $x = x_0$. For a ground-based system, t_{air} is zero and $v_{\text{rms}} = v_{\text{sub}}$. These equations are strictly valid for monostatic systems,

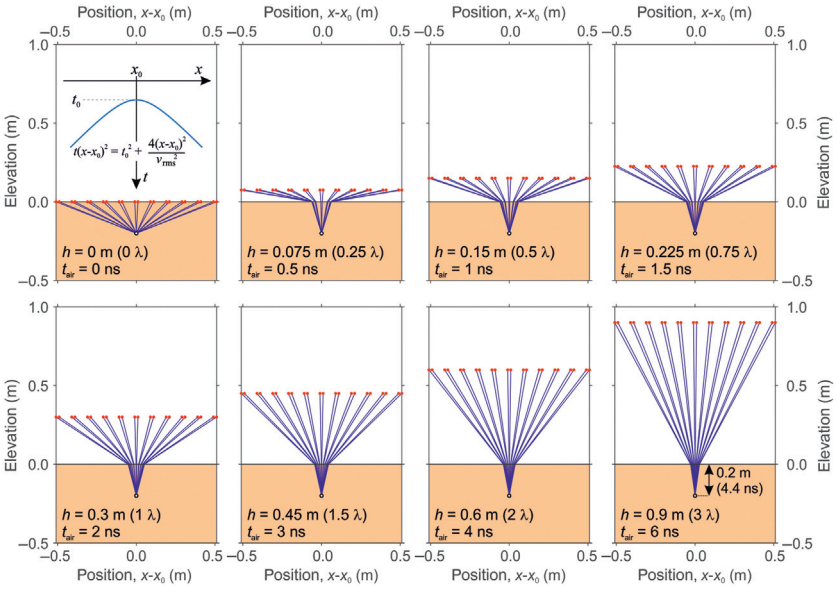

Figure 1. Raypaths modeled for a point diffractor, placed at a depth of 0.2 m in a subsurface with constant $v_{\text{sub}} = 0.09$ m/ns. Each panel shows antennas (red circles) raised to successively increased height, from 0 to 0.9 m, and the vertical traveltime t_{air} through the air gap. The additional annotation in the lower-right panel shows the vertical traveltime, 4.4 ns, between the diffractor and ground surface. A schematic representation of equation 1 is inset in the upper-left panel, accurate for ground-based antennas and constant v_{sub}.

DOI:10.1190/geo2021-0602.1

with zero transmitter-receiver offset, but nonetheless remain widely applied for finite-offset bistatic systems.

The term v_{rms} can be evaluated using several analytic methods, such as curve-fitting approaches and semblance-based velocity analysis (Booth and Pringle, 2016). With pairs of v_{rms} and t_0 available, v_{sub} can be approximated using Dix's equation (Dix, 1955):

$$v_{sub} \approx \sqrt{\frac{v_{rms}^2 t_0 - v_{air}^2 t_{air}}{t_0 - t_{air}}}, \tag{3}$$

which can be used recursively to derive the vertical variation of v_{sub} if $v_{rms}:t_0$ pairs are available.

Equation 1 is exactly hyperbolic for ground-based systems and constant, isotropic, v_{sub}. In layered velocity models, nonhyperbolic traveltime terms are introduced because refraction across interfaces is neglected (i.e., straight rays are assumed). Because traveltimes deviate from those predicted by equation 1, velocity estimates derived with it are inaccurate with respect to the true v_{sub}. This is exacerbated where $|x - x_0|$ is large with respect to the vertical distance between the antennas and the target (i.e., the sum of flight height and target depth). These errors can be circumvented using higher-order terms in traveltime approximations (e.g., Causse, 2004; Causse and Sénéchal, 2006) or through full-waveform inversion (e.g., Jazayeri et al., 2018), but these are less widespread in practice than assuming hyperbolic traveltimes and accepting some velocity error. However, strong refraction across the air-ground likely increases the severity of these errors.

In addition, there are systematic velocity errors that should be considered for any practical velocity analysis. A diffracting target with a finite radius causes v_{sub} to be biased fast (Shihab and Al-Nuaimy, 2005; Ristic et al., 2009) and v_{sub} is exaggerated further if the intersection between the long axis of an elongate diffractor (e.g., a pipe) and the profile direction is not orthogonal. Conversely, many velocity analysis approaches (e.g., curve-matching and semblance) consider the traveltimes of the highest amplitude cycles of the GPR wavelet and therefore cause v_{sub} to be biased slow; velocity is expressed more accurately by first-break traveltimes (Booth et al., 2010; Booth and Pringle, 2016). Although the impact of these is appreciated, the relative significance of velocity errors from a drone-based survey platform is currently unexplored.

DATA SIMULATION

Two approaches were adopted to simulate drone-mounted GPR acquisitions using different flight heights and a range of v_{sub}. First, a simple ray-tracing approach was used to illustrate the distortion of diffracted raypaths and the origins of velocity errors. Second, finite-difference models were implemented in gprMax (Warren et al., 2016) to capture the near-field behavior of a finite-frequency wavefield and a more realistic antenna radiation pattern.

Methods: Ray-based synthetics

Traveltimes were computed for a point diffractor at a depth of 0.2 m in a homogeneous isotropic half-space. Transmitting and receiving antennas were offset at 0.02 m, which is smaller than might be used in practice but used here to highlight the contribution to velocity errors of refraction effects rather than nonzero antenna separation. Antenna midpoint positions extended to ±0.5 m on either side of the diffractor, sampling every 0.02 m. Responses were modeled with drone flight height h ranging from 0 to 0.9 m. These heights correspond to values up to three times the wavelength λ in air of a 1000 MHz wavelet; although wavelength has no practical relevance in a ray-based simulation, we report h/λ ratios to compare with previous studies and for reference to observations from later finite-difference models. The term v_{sub} was increased in 0.01 m/ns increments from 0.07 to 0.13 m/ns, and raypaths were calculated by applying Snell's law at the air-ground interface.

Figure 1 shows modeled raypaths for all h values and $v_{sub} = 0.09$ m/ns. The ground-based model (Figure 1a) shows the straight rays expected for constant v_{sub}. Low drone flight heights introduce significant ray bending across the air-ground interface which gradually decreases with increasing h. The corresponding traveltime curves (Figure 2a) highlight the distortion from the diffraction hyperbola recorded by ground-based antennas. For models with $h > 0$, the ground-going leg of the raypaths shows little variation from the vertical, hence the corresponding diffractions are time-shifted variants of a hyperbola originating at the air-ground interface. In all cases, the shift is approximately 4.4 ns, corresponding to the vertical two-way traveltime between the air-ground interface and the diffractor (Figure 2b). This implies that the refraction effects prevent v_{sub} from significantly influencing the curvature of the diffraction response.

Results: Ray-based synthetics

The term v_{rms} is estimated for each model using a linear regression to diffraction traveltimes within an aperture extending ±0.4 m on either side of diffractor position, expressed in Figure 2c on $t^2 - x^2$ axes. The reciprocal gradient of the best-fit straight line (dashed black lines) defines $1/2v_{rms}^2$, and its intercept t_0^2. Being exactly hyperbolic, traveltimes for ground-based antennas are fit

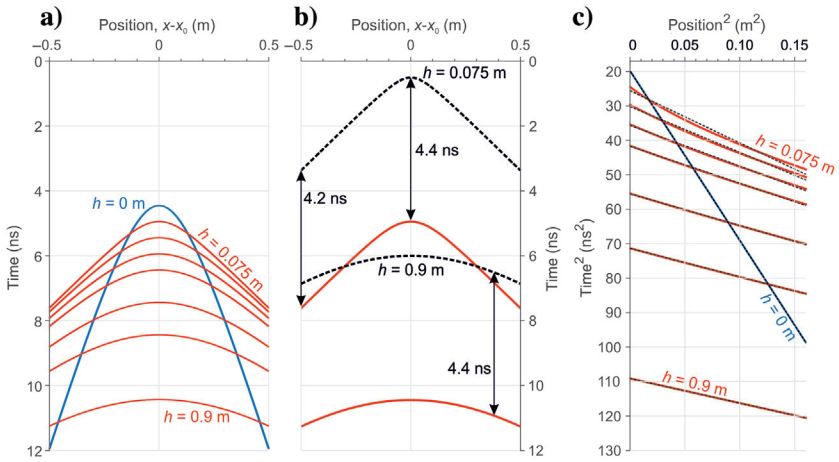

Figure 2. Ray-based traveltime curves for models in Figure 1. (a) Curves for ground-based (blue; $h = 0$) and airborne (red; $h > 0$) antennas. (b) End-member curves from (a), compared with diffraction hyperbolas (dashed black lines) from a diffracting target placed at the ground surface. Each pair of curves is shifted by approximately 4.4 ns. (c) Expression of curves in (a) on $t^2 - x^2$ axes and best-fit straight lines (dashed black lines) for each.

DOI:10.1190/geo2021-0602.1

perfectly, however nonhyperbolic terms for $h > 0$ introduce curved $t^2 - x^2$ responses which are most evident for $h \leq 0.3$ m. The term v_{sub} was estimated for each case by substituting $v_{rms} : t_0$ into Dix's equation, together with t_{air} (annotated in Figure 1) and $v_{air} = 0.3$ m/ns. Figure 3a shows v_{rms} and the resulting v_{sub}, the latter expressed as a percentage error in Figure 3b.

All v_{sub} estimates are biased fast, but the largest errors are shown for the lowest h (e.g., >50% overestimate for $h = 0.075$ m and 10% for $h = 0.9$ m). Equivalent overestimates for all modeled v_{sub} (Figure 3c) suggest that the velocity mismatch decreases with increasing h and v_{sub}. For the fastest velocity case, overestimates are always <40% and approximately 7% for the highest flight heights. However, overestimates can approach 100% for the cases of $v_{sub} \leq 0.08$ m/ns and low flight heights.

The analysis was repeated for diffractors placed at a depth of 0.6 and 1.0 m (Figure 3d and 3e, respectively). For the 0.6 m depth case, v_{sub} overestimates are typically <10% for faster v_{sub} and/or greater flight height. The overestimate seldom exceeds 6% for the 1.0 m depth case, but targets here would not be widely considered suitable for imaging with 1000 MHz antennas. Therefore, the errors in Figure 3b are more illustrative of a typical best-case scenario for this antenna frequency.

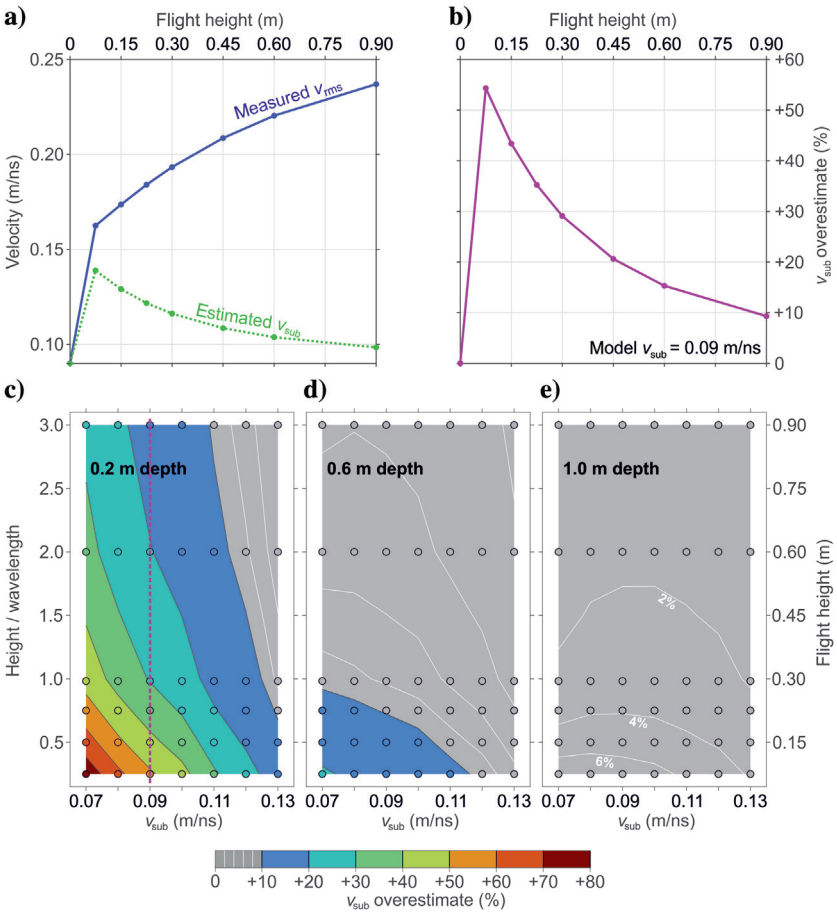

Figure 3. Measured velocities and errors with changing flight height. (a) The v_{rms} measured from $t^2 - x^2$ analysis (solid blue line) and the estimated v_{sub} (dashed green line) after substitution into Dix's equation. (b) Percentage overestimate of v_{sub}, with respect to model value of 0.09 m/ns. (c-e) Overestimates of a range of v_{sub} values for point diffractors at a depth of 0.2, 0.6, and 1.0 m, respectively. Contours are filled at 10% intervals, with white contours appearing at intervals of 2% within the 0%–10% range. The dashed pink line in (c) corresponds to the data in (b). Throughout, wavelength annotations are made to facilitate comparison with later FDTD synthetics.

Methods: Finite-difference time-domain synthetics

Ray-based modeling illustrates the challenges for diffraction-based velocity analysis but neglects realistic aspects of GPR propagation. As ray-based synthetics are infinite-frequency models, they impose far-field conditions and thus plane-wave arrivals, yet shallow targets could be present in the near field (e.g., within a small number of wavelengths; Warren and Giannopoulos, 2012) where wavefront curvature is significant. Furthermore, ray-based arrivals were weighted equally in the linear regression, whereas amplitudes in real data are affected by geometric spreading, attenuation losses and, in particular, the anisotropic radiation pattern of GPR antennas. The lattermost is likely to be particularly significant given the obliquity of the far-offset raypaths implied for low h values in Figure 1.

Finite-difference time-domain (FDTD) synthetics were undertaken using gprMax (Warren et al., 2016). A 3D domain of dimensions $[x, y, z] = [1.0 \times 1.0 \times 1.2]$ m was established and discretized into cells of dimensions $[\Delta x, \Delta y, \Delta z] = 0.005$ m. The modeled structure is 2.5D, continuous in the y-dimension, and represents a horizontal pipe installed in a trench (Figure 4). The pipe is a cylindrical perfect electrical conductor (pec), with a diameter of 0.1 m and centered at $[x, z] = [0.5, 0.2]$ m. The horizontal floor of the trench is 0.5 m wide, 0.3 m deep, and rises to 0.2 m at the edges of the domain. The overlying air gap extends 0.7 m above the ground surface, allowing antennas (red circles in Figure 4) to be placed at a range of h from 0 to 0.6 m. This is up to 2λ, for the 1000 MHz source wavelet center frequency that we assumed.

All physical quantities are fixed, except for the relative dielectric permittivity ε_r of the trench fill which is first set to 18.3 and then to 5.3, giving v_{sub} of 0.07 and 0.13 m/ns (the extreme velocity cases considered in ray-based simulations). The velocity through the lowermost layer is fixed at 0.010 m/ns, such that the velocity contrast at the base of the trench is ± 0.03 m/ns. Output radargrams (Figure 5) were produced at $y = 0.5$ m, with antenna midpoints spanning from 0.05 to 0.95 m, in 0.02 m intervals. Once simulated, the time step in the synthetic radargrams was downsampled via linear interpolation, from 0.0096 to 0.1 ns, to improve the efficiency of later velocity analysis calculation. The radargrams were contaminated with noise traces from a 1000 MHz field data set, scaled to give a 15 dB signal-to-noise ratio at the diffraction apex.

Results: FDTD synthetics

Velocity analysis was undertaken for each model using semblance (e.g., Stucchi et al., 2020), configured using the traveltime expression in equation 1 (Booth and Pringle, 2016). The calculation spanned an aperture of 0.4 m on either side

DOI:10.1190/geo2021-0602.1

of the apex and used an analysis window with 0.1 ns duration. Figure 5 shows output radargrams and their semblance responses; Figure 5a and 5b relates to v_{sub} of 0.07 and 0.13 m/ns, respectively, with Figure 5 rows (i–vii) showing flight heights increased from 0 to 0.6 m. The hyperbola on each radargram is the semblance-derived approximation to first-break traveltimes (ornament +). These are based on semblance picks made at the strongest semblance response, corresponding to the strongest half-cycle of the GPR wavelet (ornament ×) but corrected for approximately 0.53 ns lag from first break (Booth et al., 2010). The precision in v_{rms}, and in v_{sub} thereafter, is based on the width of the 90% semblance contour (Booth et al., 2011).

Diffraction responses in Figure 5 flatten progressively with increasing h above the air/ground interface, becoming indistinct from the response from the trench floor. Furthermore, consistent with observations in Figure 2b, they become time-shifted replicas of each other: the traveltime moveout of the diffractions differs by just 0.8 ns between Figure 5a (vii) and 5b (vii), despite the difference in the velocity models. Figure 6 shows that v_{rms} tends toward 0.3 m/ns as h increases (Figure 6a and 6c), with v_{rms} and v_{sub} becoming increasingly imprecise. For expressing v_{sub} as a fractional error (Figure 6b and 6d), reference values are increased to 0.079 and 0.134 m/ns, respectively, according to the diffraction traveltime given in Shihab and Al-Nuaimy (2005; equation 3 therein) that incorporates the finite-radius effect of our pipe geometry (specifically, with a radius-to-center-depth ratio of 0.25). For comparison, Figure 6b and 6d also includes the relative errors in v_{sub} from the ray-based models in Figure 3c.

Although Figure 6 suggests that the model v_{sub} will be overestimated for any $h > 0$, errors are generally less than in ray-based models, particularly for small h. For $h = 0.075$ m (0.25λ), simple ray-based models indicated that the slow velocities could be overestimated by 100%, yet Figure 6b suggests an overestimate no greater than approximately 5%. This is attributed to antenna radiation effects. For $\varepsilon_r > 12$, Warren and Giannopoulos (2012) indicate a reduction of >20 dB in radiated amplitudes for take-off angles exceeding 60°. For our model geometry and $h = 0.075$ m, this angle is reached when antennas are located ± 0.16 m either side of the diffractor. The effect is clear in Figure 5a (ii), in which the diffracted amplitudes decrease rapidly beyond positions ± 0.2 m from the diffraction apex meaning that arrivals outside of this aperture contribute less to the overall semblance response. This is why the semblance-derived traveltime curve is a good match to the curvature of the diffraction around its apex and diverges at its flanks. Indeed, in revisiting Figure 2c, the local gradient of the $h = 0.075$ m curve is steepest in the $[0 - 0.2]^2$ m^2 range of x^2, and a linear regression using only this range reduces the overestimate of v_{sub} from >70% to approximately 45%.

Guidance from finite-difference simulations is therefore opposite to ray-based modeling, indicating that the accuracy and precision of velocity estimates is benefited by a low flight height (Smith, 1984). Furthermore, given their flatness, the responses observed with antennas >0.3 m (1λ) high are likely more vulnerable to noise and static shifts resulting from velocity heterogeneity and/or antenna mispositioning.

FIELD DATA

The practical implications of the synthetic models were explored using GPR field data, acquired with an adaptable frame to simulate drone-based acquisitions at varying flight heights (Figure 7a). The frame is made from a polystyrene cradle and carries Sensors & Software (S&S) pulseEKKO PRO 1000 MHz antennas with 0.15 m offset between antenna centers. Consistent with a drone platform, there is no material beneath the antennas hence they radiate directly into the air. A carry handle from an S&S low-frequency antenna is attached to the frame with its adjustable legs marked in 0.05 m intervals. With the system carried at a constant level, the antennas can be elevated to different heights above the ground surface. Along-profile distances were measured using a calibrated odometer wheel, towed behind the frame.

Field data acquisition

Field data (Booth, 2021) were acquired in July 2020 on Canal Road (UK National Grid SE 22306 36370), a quiet side street in the Rodley district of Leeds, UK (Figure 7b). Restrictions imposed during the UK's COVID-19 response limited the range of accessible field locations. Nonetheless, Canal Road is of archaeological interest given its 200 year history of accessing an industrial wharf on the adjacent Leeds-Liverpool canal (Figure 7b): the modern road surface likely covers the original structure.

GPR profiles are 20 m long, although only their first 8 m are used in this paper, with a 0.01 m trace interval and repeated with h increasing from 0 to 0.35 m in increments of 0.05 m (=λ/6 for a 1000 MHz wavelet in air). The time sampling interval was 0.1 ns. Data were processed in Sandmeier ReflexW© software (version 8.5), using the sequence:

1) dewow filter (window length 2 ns),
2) Ormsby band-pass filter (corner frequencies at 200–400–1200–2400 MHz),

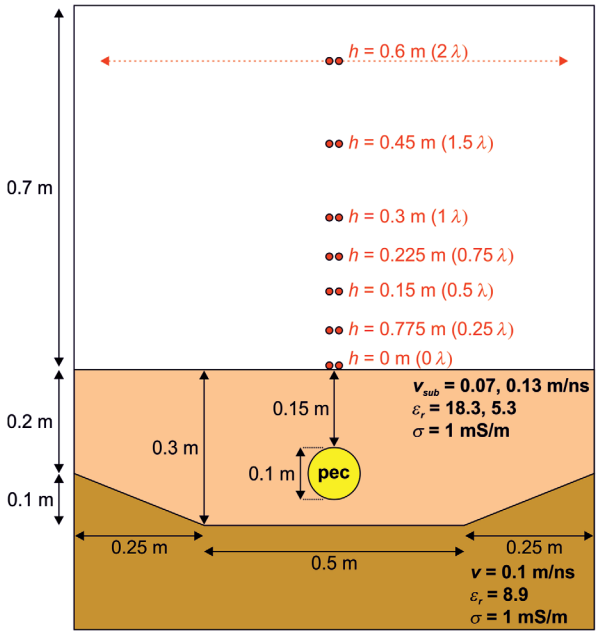

Figure 4. The [x, z] cross section through the gprMax model. A cylindrical perfect electric conductor (pec) is placed at a depth of 0.15 m in a subsurface with fixed electrical conductivity ($\sigma = 1$ mS/m) but variable v_{sub}. Antennas (red circles) span a range of x from 0.05 to 0.95 m and are positioned at h up to 0.6 m ($0 - 2\lambda$).

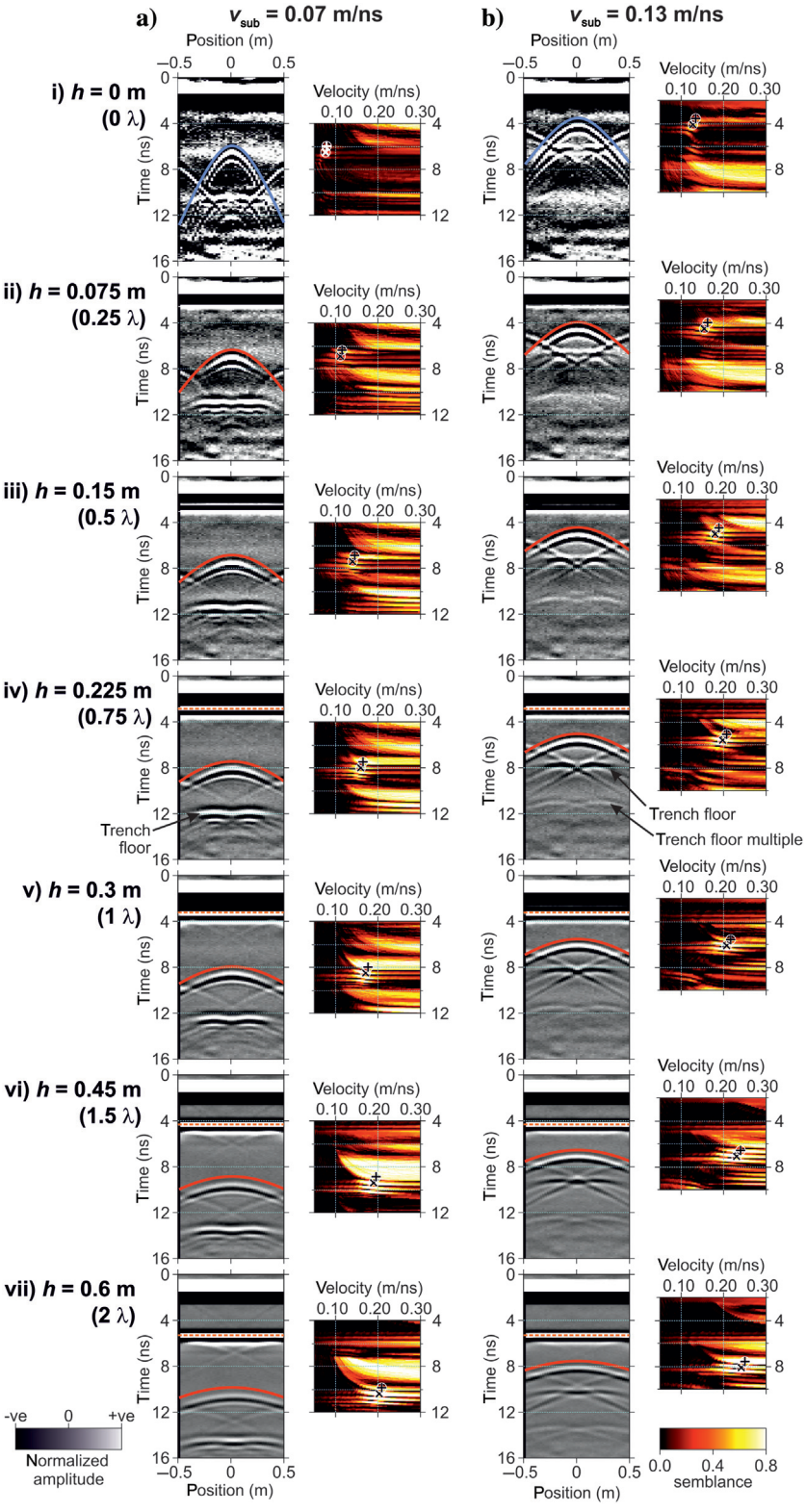

Figure 5. Synthetic radargrams and semblance responses for v_{sub} of (a) 0.07 m/ns and (b) 0.13 m/ns, and h increased (i–vii) from 0 to 0.6 m. The hyperbola in each radargram approximates first-break traveltimes using semblance picks corrected (ornament +) from peak responses (ornament ×). The dashed orange line in models with $h > 0.15$ m shows the reflection from the air-ground interface. All radargram and semblance panels share the same color scale and amplitude range.

3) time-variant "energy decay" gain function, and
4) spatial filtering; the mean trace from within successive 3 m windows is calculated and subtracted from individual traces, thus preferentially suppressing horizontal arrivals.

The noise traces with which the gprMax models (Figure 5) were contaminated are extracted from 13 to 20 ns in the ground-based profiles.

Data from the ground-based acquisition (Figure 8a), processed using the preceding sequence, revealed a sequence of subhorizontal interfaces and a series of diffractions with a regular spacing of 0.5–0.6 m intervals, rising from approximately 8 to 6 ns traveltime through the profile. Although their origin is unknown, presumed to be related to the original road foundation, they nonetheless provide targets for diffraction-based velocity analysis. Had more time been available, the acquisition of a small grid would have been valuable for ensuring that our main profile crossed the diffractions orthogonally.

A wide-angle reflection/refraction (WARR) survey (Diamanti et al., 2018; Figure 8b) was acquired to provide velocity control: the transmitter was located at 6.90 m along the profile, with the receiver position moved in 0.05 m increments from 7.05 to 8.65 m (0.15–1.85 m offset range). The semblance response to the WARR data suggests a three-layer velocity model (inset, Figure 8b). On substituting corrected semblance picks (ornament +) into Dix's equation and extrapolating the resulting velocity model across the profile, the deepest clear diffraction (position 1.35 m along the x-axis, marked with the red arrow) is interpreted to originate from the base of a layer at 0.33 ± 0.05 m depth and 0.11 ± 0.05 m thick, with $v_{sub} = 0.087 \pm 0.008$ m/ns. This v_{sub} is used as the reference velocity, against which velocity errors are later compared, although it is acknowledged that ground truth velocities and diffractor geometries are unknown.

Field data results

Recorded profiles are shown in Figure 9, displayed before (Figure 9a) and after (Figure 9b) the application of spatial filtering. For $h \geq 0.1$ m ($2\lambda/6$; Figure 9a, iii–vii), data are dominated by horizontal ringing, assumed to be reverberations between the ground surface (marked in Figure 8b) and the base of the antennas. Perturbations in the traveltime of the surface reflection suggest some inconsistency in the antennas' height, but these are typically <0.2 ns (<0.03 m) and are small compared with the depth of the target. In any case, they may represent the stability of a real drone platform. The reverberations are suppressed with the appli-

DOI:10.1190/geo2021-0602.1

cation of spatial filtering, but the subsurface structure remains greatly obscured for $h \geq 0.1$ m ($2\lambda/6$). For $h \geq 0.1$ m (1λ), some expression of the subhorizontal layering appears (e.g., at approximately 10 ns in Figure 9b, vi) but the diffractions remain obscured, and the image would be difficult to interpret without also seeing the ground-based data.

With the sparsity of available diffraction responses in the field data, velocity analysis was only performed for the diffraction at 1.35 m along the profile, for ground-based antennas and $h = 0.05$ m (Figure 10a and 10b, respectively). Semblance is calculated in a 0.1 ns window and spans an aperture of 0.25 m on either side of the diffraction apex. As anticipated, the air gap increases v_{rms}. The 13% increase (from v_{rms} of 0.0917–0.104 m/ns) is approximately half of that suggested in Figure 6c for representative flight heights but the characteristics of the real data are otherwise consistent with the FDTD synthetics.

The accuracy of v_{sub} estimates is compared against the reference model at 1.35 m (Figure 8). For the ground-based data, v_{rms} and t_0 through the overburden are 0.099 m/ns and 4.4 ns, respectively. Combining these in Dix's equation with the quantities derived in Figure 10a, v_{sub} is estimated as 0.077 ± 0.003 m/ns, within 13% of the model v_{sub}. For $h = 0.05$ m, the overburden v_{rms} must first be recalculated to allow for propagation through the air gap. Using equation 2, and assuming $t_{air} = 0.33$ns ($= 2h/v_{air}$), the $[v_{rms}:t_0]$ pair at the base of the first subsurface layer is [0.127 m/ns, 4.77 ns]. Here, Dix's equation yields an implausibly slow v_{sub} estimate of 0.036 m/ns, although this is highly sensitive to uncertainty ranges: when v_{rms} is increased by 0.009 m/ns to its upper uncertainty bound, the implied v_{sub} is increased to 0.085 m/ns. Dix's equation is vulnerable to uncertainties particularly where traveltime differences in the denominator of the expression are small. However, this is exacerbated for drone-based surveying, where the addition of an air gap adds further measurement uncertainty to the analysis.

DISCUSSION

Drone platforms offer logistical benefits for GPR surveying, but the imaging and analysis of diffraction hyperbolas are vulnerable to errors related to strong refraction effects at the air-ground interface. Recommendations for optimizing drone flight height are contradictory when made using different approaches: ray-based models suggest a fly high strategy to minimize refraction but the more realistic FDTD approach, using a full-waveform simulation, indicates that flying low benefits the precision and accuracy of veloc-

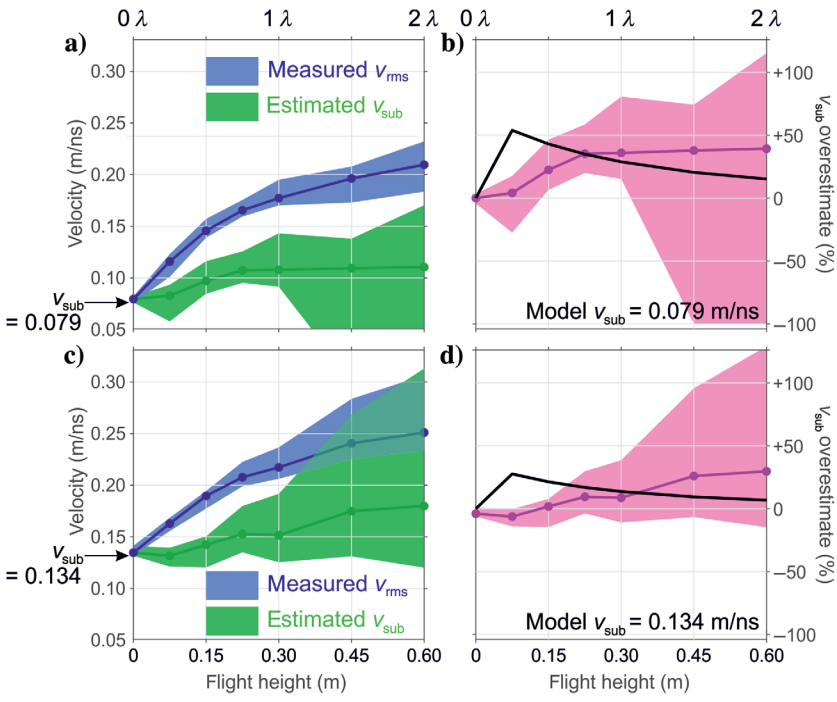

Figure 6. Semblance-derived v_{rms} and v_{sub} for the models in Figure 5. Colored areas show velocity estimates and their precision for (blue) v_{rms} and (green) modified v_{sub} of (a and b) 0.079 m/ns and (c and d) 0.134 m/ns. Pink areas in (b and d) show the percentage overestimate in model v_{sub}, with the black lines showing the equivalent errors from ray-based models in Figure 3c.

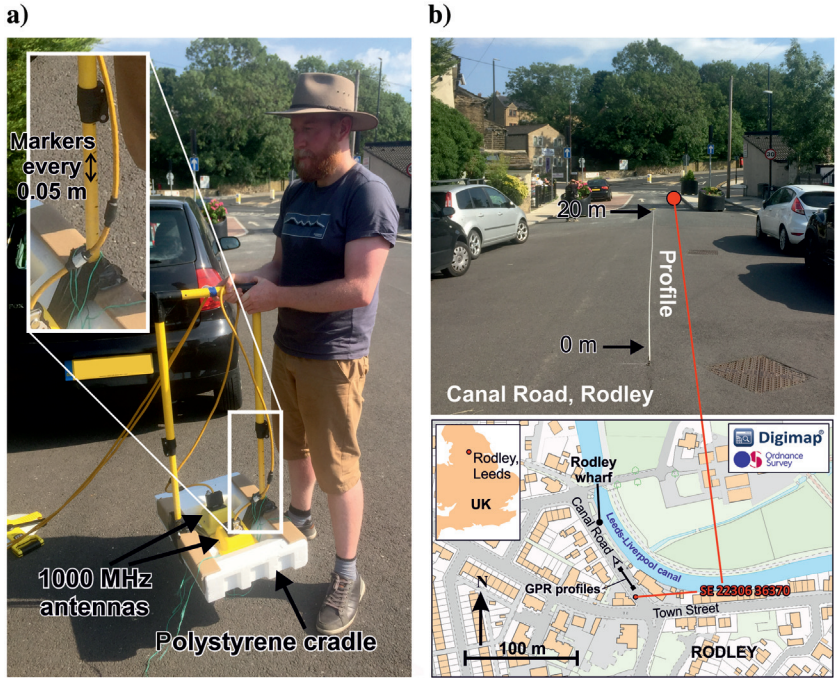

Figure 7. Field data acquisition. (a) The 1000 MHz center frequency antennas placed within a polystyrene frame to simulate drone-mounted GPR surveys. Inset: markers to simulate different flight heights. (b) Survey location on Canal Road, Rodley, UK. Upper: View southeast along Canal Road and the position of 20 m long profiles. Lower: Site map from UK Ordnance Survey showing Canal Road and its proximity to the Leeds-Liverpool canal and a defunct wharf. Viewpoint for upper panel is marked.

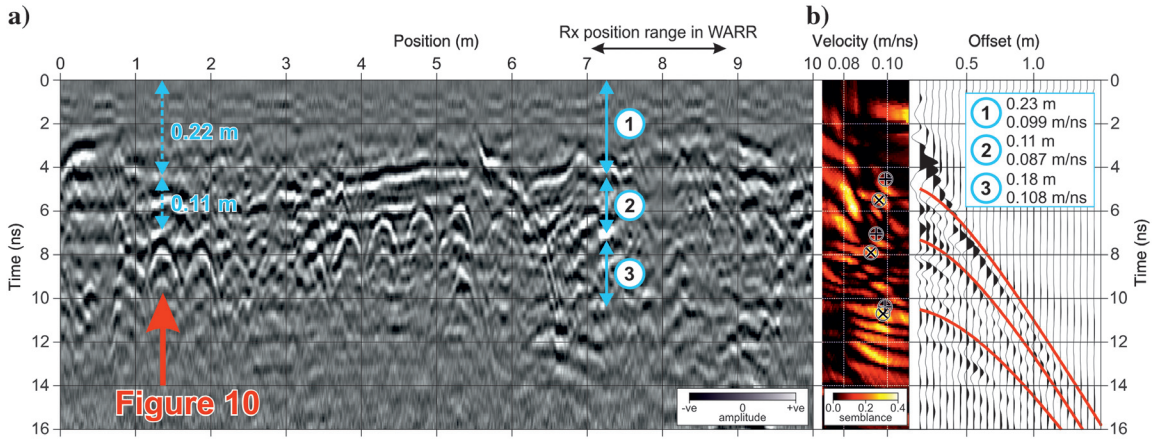

Figure 8. Ground-based GPR data from Canal Road surveys. (a) First 10 m of ground-based GPR profile. A diffraction at 1.35 m position, at approximately 7 ns traveltime, beneath subhorizontal layering (depth at approximately 0.33 m) is highlighted for later analysis. (b) WARR data, spanning a midpoint range of 7.0–7.8 m, and its semblance response. Reflection hyperbolas (red) are defined by $[v_{\mathrm{rms}} : t_0]$ shown by ornament + in the semblance panel. Inset: three-layer velocity:thickness model, accurate to approximately $\pm 15\%$, based on the 90% semblance contour.

Figure 9. The GPR profiles from Canal Road survey, with h increased from (i) 0 to (viii) 0.35 m ($= 7\lambda/6$). Data are shown (a) before and (b) after the application of spatial filtering. Red boxes show the indication of subhorizontal layering for large h, and orange annotations highlight the reflection from the ground surface at the heights that it could be resolved from the direct air wave.

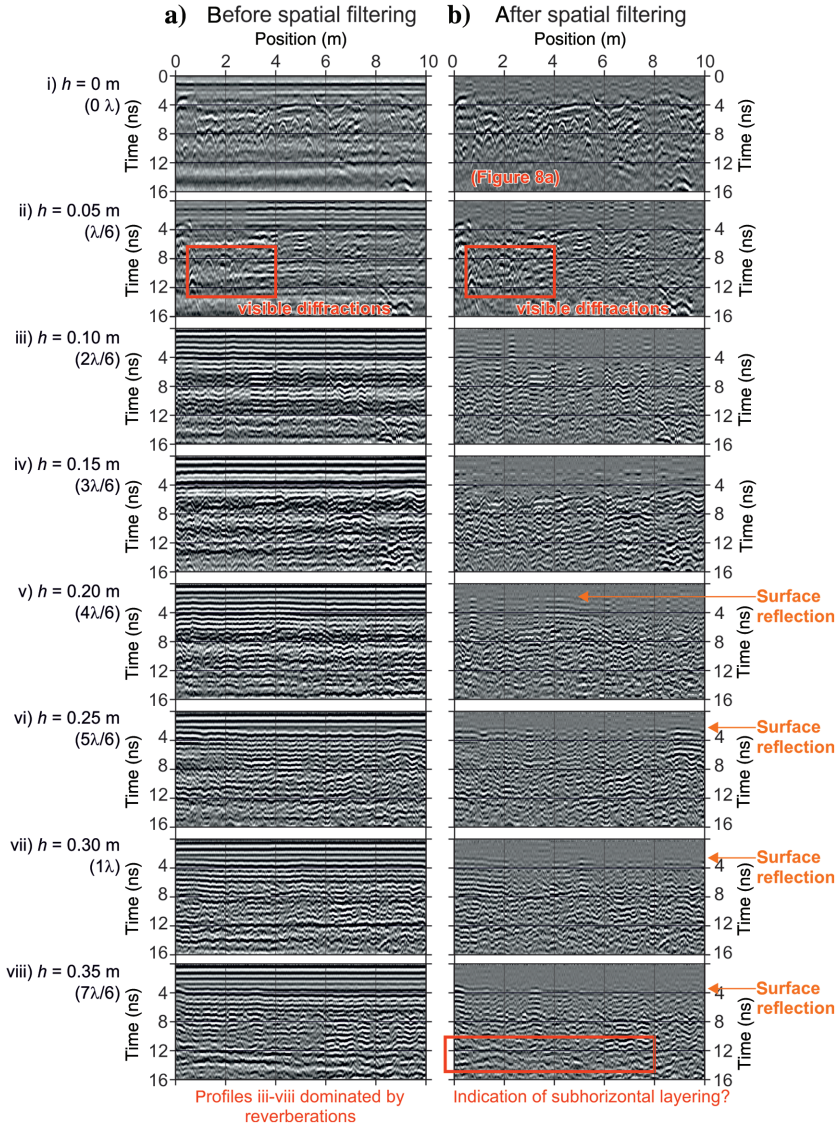

DOI:10.1190/geo2021-0602.1

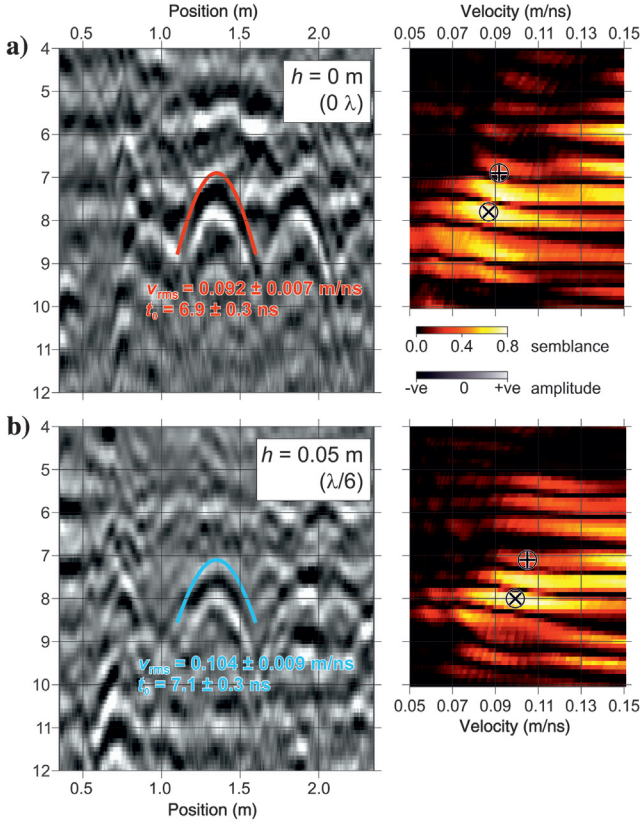

Figure 10. Semblance analysis of diffraction highlighted in Figure 8, for (a) ground-based antennas and (b) antennas at $h = 0.05$ m. Diffraction hyperbolas are defined by $[v_{\text{rms}} : t_0]$ shown by ornament + in the semblance panels, across the 0.25 m aperture either side of the diffraction apex. Annotated velocity precision is based on the width of the 90% semblance contour.

ity estimates. Field data also suggest that a low flight height is preferable, although our data set does little to recommend drone-based diffraction imaging overall. Although data quality in our lowest flight height (0.05 m, $\lambda/6$) compared well with that from a conventional ground-based acquisition, the obscurity of diffractions in most of the profiles suggests that the accuracy of diffraction-based velocity analysis may be of secondary importance to the question of whether diffractions can be recognized at all.

Limited visibility of real data diffractions

Two considerations may explain the limited visibility of diffractions in the real data. First, Figure 5 showed that characteristic diffraction responses will flatten rapidly with increasing flight height, to the point where they may become indistinct from subhorizontal reflectivity and, potentially, the reflection from the air-ground interface (marked where visible in Figure 5). With reduced curvature, the diffraction is more vulnerable to further traveltime perturbations related to (e.g.) microtopography on the air-ground interface and/or small-scale velocity anomalies in the overburden. A further feature of our real data was the strong reverberations in the air gap: these were suppressed using consistent spatial filters that preferentially attenuated horizontal trends; hence, it is possible that diffraction amplitudes also were attenuated in this step.

The second consideration is the spatial resolution of the wavelet, expressed by its Fresnel diameter F_d:

$$F_d = v_{\text{rms}}(2t_0)^{\frac{1}{2}}, \tag{4}$$

where τ is the half-period of the dominant frequency (Lindsey, 1989). For a wavelet of any given frequency, propagating for a fixed traveltime, the spatial resolution will be poorer (i.e., F_d increases) for increased v_{rms}. For the synthetic results in Figure 6a, assuming $\tau = 0.5$ ns and flight height increased from 0 to 0.6 m, v_{rms} increases from approximately 0.08 to 0.21 m/ns, and t_0 from 6 to 11 ns. This leads F_d to increase from 0.2 to 0.7 m. The expression of diffracting targets may fundamentally change for drone-based antennas compared with the same targets' appearance in a ground-based system. For our field data set, the sequence of closely spaced discrete diffractions in Figure 9 may become the specular surface seen in our highest flight height.

Measures to improve velocity accuracy

In situations where diffraction hyperbolas can be resolved, the accuracy of the implied velocity models must still be addressed. If interpretations are to be made using the hyperbolic traveltime definition in equation 1, we advise using a narrow aperture to mitigate nonhyperbolic traveltime terms. However, the resulting improvement in accuracy will be a compromise with velocity precision because precision is superior when a target event expresses greater traveltime moveout (Booth et al., 2011). Furthermore, this may impact the application of automated detection algorithms (e.g., Dou et al., 2017) that rely on consistent expressions of hyperbolas to be successful.

The compromise between accuracy and precision can be avoided using higher-order definitions (e.g., Alkhalifah, 1997; Causse, 2004) of traveltime moveout. A fourth-order moveout definition,

$$t(x - x_0) \approx \sqrt{t_0^2 + \frac{4(x - x_0)^2}{v_{\text{rms}}^2} + C(x - x_0)^4}, \tag{5}$$

based on the definition of Alkhalifah (1997), accumulates all nonhyperbolic traveltime terms into parameter C. When applied to Figure 5a (vii) ($h = 2\lambda$), the residual traveltime between the observed diffraction moveout and that defined by equation 5 is minimized for $v_{\text{rms}} = 0.2018$ m/ns, approximately 3% lower than the value (0.2075 m/ns) implied by the hyperbolic traveltime definition. However, on using this v_{rms} in Dix's equation, the implied v_{sub} is 0.1133 m/ns, an overestimate of 60% in the model value of 0.079 m/ns. This result implies that the degree of nonhyperbolic moveout may even be too severe for a fourth-order traveltime definition, without further restriction to the analysis aperture.

The most accurate approaches to velocity analysis may therefore involve full waveform inversion (Jazayeri et al., 2018), or a migration velocity analysis routine (St. Clair and Holbrook, 2017) that seeks to best focus diffraction responses. Although these are beyond the scope of this study, we caution that they intrinsically rely on being able to recognize diffraction features to begin with and, as shown in our field data set, this may not routinely be the case for all but the lowest drone flight heights.

Outlook

Drone-based GPR applications merit further investigation, but imaging and/or quantitative use of diffractions may be limited to

cases in which the flight height is as close to the ground as practically possible. In other settings, the drone platform may be more promising, for example, when used for imaging subhorizontal specular reflectivity because the near-vertical propagation of reflected energy will minimize refraction effects at the air-ground interface. Low-frequency airborne radar methods are already well established in glaciology, and the drone-based platform may be less problematic in this setting given the small refractive index at the air-snow/ice interface (e.g., Tan et al., 2018; Mankoff et al., 2020). However, because the degree of refraction across the ground surface is a frequency-independent effect, we expect that the low-frequency applications in more conventional terrestrial settings will still be impacted by similar velocity errors. We would therefore advise that a drone acquisition is performed with a low flight height and is accompanied, if possible, by a ground-based survey to benchmark any loss of image quality and provide more reliable velocity control.

CONCLUSION

Drone technology offers logistical benefits for several geophysical survey methods, and numerous researchers have explored its applicability for GPR acquisition. Established guidance suggests that the optimal flight height for the antennas is between 0.5 and 1.5 times the GPR wavelength in air, but no study has to date assessed this recommendation for its impact on diffraction-based velocity analysis. This impact is potentially significant, owing to strong refraction effects at the air-ground interface

FDTD simulations suggest that the velocity analyses are more accurate and precise if the drone is flown as close to the ground surface as possible. Although this geometry risks stronger ray bending, the effect of nonhyperbolic terms is minimized by the anisotropic radiation pattern of the GPR antenna. Furthermore, higher flight heights produce flatter diffraction trajectories, risking diffraction responses being overlooked, and/or indistinguishable from nearby subhorizontal reflectivity.

A field data set simulating a drone-based acquisition highlights the vulnerability of diffractions being overlooked. Antennas are raised to over one wavelength (0.3 m) from the ground surface, yet diffractions are only visible in the lowest-flying data set (0.05 m off the ground). A combination of reverberation in the air gap and a decrease in the horizontal resolution of the wavelet likely explains this poor performance. We conclude that the drone platform merits further investigation for GPR applications, including measures to improve velocity accuracy, but suggest that it is currently more suitable for imaging specular reflectivity than it is the quantitative analysis of diffraction responses.

ACKNOWLEDGMENTS

TMK undertook the preliminary stages of this research while studying M.Sc. Exploration Geophysics at the University of Leeds. Advice on gprMax simulation from A. Giannopoulos was gratefully received. The manuscript was greatly improved with constructive comments from associate editor G. Tsoflias, reviewer N. Diamanti, and two anonymous reviewers.

DATA AVAILABILITY

GPR field data are available to download from the figshare repository, https://doi.org/10.6084/m9.figshare.16573025.v1.

REFERENCES

Alkhalifah, T., 1997, Velocity analysis using non-hyperbolic moveout in transversely isotropic media: Geophysics, **62**, 1683–2002, doi: 10.1190/1.1444285.

Annan, A. P., 2005, Ground-penetrating radar, *in* D. K. Butler, ed., Near surface geophysics: SEG 13, 357–438.

Booth, A., 2021, Profiles of ground-penetrating radar data simulating a drone-mounted acquisition, figshare, Dataset, doi: 10.6084/m9.figshare.16573025.v1.

Booth, A. D., R. A. Clark, and T. Murray, 2010, Semblance response to a ground-penetrating radar wavelet and resulting errors in velocity analysis: Near Surface Geophysics, **8**, 235–246, doi: 10.3997/1873-0604.2010008.

Booth, A. D., R. A. Clark, and T. Murray, 2011, Influences on the resolution of GPR velocity analyses and a Monte Carlo simulation for establishing velocity precision: Near Surface Geophysics, **9**, 399–411, doi: 10.3997/1873-0604.2011019.

Booth, A. D., and J. K. Pringle, 2016, Semblance analysis to assess GPR data from a five-year forensic study of simulated clandestine graves: Journal of Applied Geophysics, **125**, 37–44, doi: 10.1016/j.jappgeo.2015.11.016.

Bradford, J. H., J. Nichols, T. D. Mikesell, and J. T. Harper, 2009, Continuous profiles of electromagnetic wave velocity and water content in glaciers: An example from Bench Glacier, Alaska, USA: Annals of Glaciology, **50**, 1–9, doi: 10.3189/172756409789097540.

Causse, E., 2004, Approximations of reflection travel times with high accuracy at all offsets: Journal of Geophysics and Engineering, **1**, 28–45, doi: 10.1088/1742-2132/1/1/004.

Causse, E., and P. Sénéchal, 2006, Model-based automatic dense velocity analysis of GPR field data for the estimation of soil properties: Journal of Geophysics and Engineering, **3**, 169–176, doi: 10.1088/1742-2132/3/2/008.

Cerquera, M. R. P., J. D. C. Montaño, and I. Mondragón, 2017, UAV for landmine detection using SDR-based GPR technology, *in* H. Canbolat, ed., Robots operating in hazardous environments: IntechOpen, Chap. 2, doi: 10.5772/intechopen.69738.

Chandra, M., and T. J. Tanzi, 2018, Drone-borne GPR design: Propagation issues: Comptes Rendus Physique, **19**, 72–84, doi: 10.1016/j.crhy.2018.01.002.

Diamanti, N., and A. P. Annan, 2013, Characterizing the energy distribution around GPR antennas: Journal of Applied Geophysics, **99**, 83–90, doi: 10.1016/j.jappgeo.2013.08.001.

Diamanti, N., and A. P. Annan, 2017, Air-launched and ground-coupled GPR data: 11th European Conference on Antennas and Propagation (EUCAP), 1694–1698.

Diamanti, N., A. P. Annan, and J. D. Redman, 2017, Concrete bridge deck deterioration assessment using ground penetrating radar (GPR): Journal of Environmental and Engineering Geophysics, **22**, 121–132, doi: 10.2113/JEEG22.2.121.

Diamanti, N., E. J. Elliott, S. R. Jackson, and A. P. Annan, 2018, The WARR machine: System design, implementation and data: Journal of Environmental and Engineering Geophysics, **23**, 469–487, doi: 10.2113/JEEG23.4.469.

Dix, C. H., 1955, Seismic velocities from surface measurements: Geophysics, **20**, 68–86, doi: 10.1190/1.1438126.

Dou, Q., L. Wei, D. R. Magee, and A. G. Cohn, 2017, Real-time hyperbola recognition and fitting in GPR data: IEEE Transactions on Geoscience and Remote Sensing, **55**, 51–62, doi: 10.1109/TGRS.2016.2592679.

Edemsky, D., A. Popov, I. Prokopovich, and V. Garbatsevich, 2021, Airborne ground penetrating radar, field test: Remote Sensing, **13**, 667, doi: 10.3390/rs13040667.

Eriksen, A., J. Gascoyne, and W. Al-Nuaimy, 2004, Improved productivity and reliability of ballast inspection using road-rail multi-channel GPR: Railway Engineering 2004, 6–7th July 2004, Commonwealth Institute, London, UK.

García-Fernández, M., Y. Álvarez López, A. De Mitri, D. Castrillo Martínez, G. Álvarez-Narciandi, and F. Las-Heras Andrés, 2020, Portable and easily-deployable air-launched GPR scanner: Remote Sensing, **12**, 1833, doi: 10.3390/rs12111833.

García-Fernández, M., Y. Álvarez López, B. Gonazález Valdés, Y. Rodríguez Vaquiero, F. Las-Heras Andrés, and A. Pino García, 2018, Synthetic aperture radar imaging system for landmine detection using a ground penetrating radar on board an unmanned aerial vehicle: IEEE Access, **6**, 45100–45112, doi: 10.1109/ACCESS.2018.2863572.

Hammack, R., G. Veloski, M. Schlagenhauf, R. Lowe, A. Zorn, and L. Wylie, 2020, Using drone-mounted geophysical sensors to map legacy oil and gas infrastructure: Unconventional Resources Technology Conference, SEG, Global Meeting Abstracts, URTeC: 2876.

Jazayeri, S., A. Klotsche, and S. Kruuse, 2018, Improved resolution of pipes with full waveform inversion of common-offset GPR data using PEST: Geophysics, **83**, no. 4, H27–H41, doi: 10.1190/geo2017-0617.1.

Lane, J. W., Jr., 2019, Development of a drone-deployed ground-penetrating radar system for non-contact bathymetry of freshwater systems: AGU-SEG Airborne Geophysics Workshop.
Lindsey, J. P., 1989, The Fresnel zone and its interpretative significance: The Leading Edge, **8**, 33–39, doi: 10.1190/1.1439575.
Mankoff, K. D., D. van As, A. Lines, T. Bording, J. Elliott, R. Kraghede, H. Cantalloube, H. Oriot, P. Dubois-Fernandez, O. Ruault du Pleiss, A. V. Christiansen, E. Auken, K. Hansen, W. Colgan, and N. B. Karlsson, 2020, Search and recovery of aircraft parts in ice-sheet crevasse fields using airborne and in situ geophysical sensors: Journal of Glaciology, **66**, 496–508, doi: 10.1017/jog.2020.26.
Ofcom, 2019, Requirements and guidance notes for ground probing and wall probing radar: UK Government Office of Communications, Report OfW 350.
Pieraccini, M., N. Rohjani, and L. Miccinesi, 2017, Comparison between horn and bow-tie antennas for ground penetrating radar: 9th International Workshop on Advanced Ground Penetrating Radar (IWAGPR).
Ristic, A., D. Petrovacki, and M. Govedarica, 2009, A new method to simultaneously estimate the radius of a cylindrical object and the wave propagation velocity from GPR data: Computers & Geosciences, **35**, 1620–1630, doi: 10.1016/j.cageo.2009.01.003.
Saarenketo, T., and T. Scullion, 2000, Road evaluation with ground penetrating radar: Journal of Applied Geophysics, **43**, 119–138, doi: 10.1016/S0926-9851(99)00052-X.
Shihab, S., and W. Al-Nuaimy, 2005, Radius estimation for cylindrical objects detected by ground penetrating radar: Subsurface Sensing Technologies and Applications, **6**, 151–166, doi: 10.1007/s11220-005-0004-1.
Šipoš, D., and G. Gleich, 2020, A lightweight and low-power UAV-borne ground penetrating radar design for landmine detection: Sensors, **20**, 2234, doi: 10.3390/s20082234.
Smith, G. S., 1984, Directive properties of antennas for transmission into a material halfspace: IEEE Transactions on Antennas and Propagation, **32**, 232–246, doi: 10.1109/TAP.1984.1143307.
St. Clair, J., and W. S. Holbrook, 2017, Measuring snow water equivalent from common-offset GPR records through migration velocity analysis: The Cryosphere, **11**, 2997–3009, doi: 10.5194/tc-11-2997-2017.
Stucchi, E., A. Ribolini, and A. Tognarelli, 2020, High-resolution coherency functions for improving the velocity analysis of ground-penetrating radar data: Remote Sensing, **12**, 2146, doi: 10.3390/rs12132146.
Tan, A. E.-C., K. Eccleston, I. Platt, I. Woodhead, W. Rack, and J. McCulloch, 2018, Microwave measurements of snow over sea-ice in Antarctica: Proceedings of the 12th International Conference on Electromagnetic Wave Interaction with Water and Moist Substances (ISEMA), IEEE, doi: 10.1109/ISEMA.2018.8442319.
Valentine, S., 2019, Geophysical trespass, privacy and drones in oil and gas exploration: Journal of Air Law and Commerce, **84**, 507.
Warren, C., and A. Giannopoulos, 2012, Investigation of the directivity of a commercial ground-penetrating radar antenna using a finite-difference time-domain antenna model: 14th International Conference on Ground Penetrating Radar, IEEE, 226–231.
Warren, C., A. Giannopoulos, and I. Giannakis, 2016, gprMax: Open source software to simulate electromagnetic wave propagation for ground penetrating radar: Computer Physics Communications, **209**, 163–170, doi: 10.1016/j.cpc.2016.08.020.
Zan, Y., Z. Li, G. Su, and X. Zhang, 2016, An innovative vehicle-mounted GPR technique for fast and efficient monitoring of tunnel lining structural conditions: Case Studies in Nondestructive Testing and Evaluation, **6**, 63–69, doi: 10.1016/j.csndt.2016.10.001.

Biographies and photographs of the authors are not available.